RANS modeling for compressible and transitional flows

By F. S. Lien[1], G. Kalitzin AND P. A. Durbin

Recent LES suggested that the turbulence fluctuation in the wall-normal direction v' plays an important role in the evolution of transition. This motivates the use of $v^2 - f$ model for turbomachinery flows, in which different types of transition co-exist. An 'ad hoc' Reynolds-number-dependent term is added to $C_{\varepsilon 1}$ in the ε-equation in order to reduce the level of near-wall dissipation rate. As a result, the onset and length of transition are greatly improved for a moderate level of free-stream turbulence intensity. However, the peak of streamwise turbulence intensity within the transition zone is underestimated. The implication of this is that the intermittency effect needs to be incorporated into the model – for example, based on the 'conditioned Navier-Stokes equation' which splits the equation into turbulent and nonturbulent parts – in order to capture the correct physical mechanism of transition. Another objective of this study is to resolve the issue of whether the 'elliptic relaxation' model can be used for supersonic flows. The results for the RAE2822 transonic airfoil will demonstrate that a good agreement with experimental data has been achieved. This is because the pressure-strain term ($\sim f$), though elliptic in nature, acts simply as a source term in the $\overline{v^2}$-equation, which is not associated with the convection process.

1. Introduction

Turbomachinery flows, even in simple linear cascades, pose a range of physical, geometrical, and numerical challenges. The former includes the passing-wake/boundary-layer interaction, shock/boundary-layer interaction, rotation, tip and passage vortices, impingement, separation, and transition. Because the turbulence level in compressors and turbines is typically about $5 - 10\%$ (except in the wakes, where the turbulence level can be as high as $15 - 20\%$), three types of transition are commonly observed in gas turbine engines. The first is called 'bypass transition', in which Tollmien-Schlichting waves are completely bypassed and turbulent spots are directly produced within the boundary layer by the influence of free-stream turbulence. The second, termed 'separated-flow' transition, often occurs in the free shear layer close to the reattachment point of a laminar separation bubble. The third, caused by the periodic passing of wakes from upstream airfoils, is called 'wake-induced' transition. Moreover, pressure gradients due to curvatures of blade surfaces also influence the evolution of transition. For example, favorable pressure gradient tends to delay transition and, when the acceleration parameter $K = \nu/U_\infty^2(dU_\infty/dx) > 3 \times 10^{-6}$,

1 University of Waterloo, Canada

results in 'relaminarization'. On the other hand, adverse pressure gradient tends to promote transition. Only the first two types of transition will be investigated here.

Modeling transition within the RANS approach was mostly based on the low-Reynolds-number eddy-viscosity formulation. Examples include Launder & Sharma's $k-\varepsilon$ model (1974) and Craft's *et al.* $k-\varepsilon-A_2$ model (1995). Although these two models can give credible results for a flow over a flat plate with a sharp leading edge at zero pressure gradient, the transition was predicted too early when the flow is accelerated/decelerated, and in certain circumstances numerical instabilities also occurred (see Chen *et al.*, 1998a & 1998b, for details). In order to improve these deficiencies, several researchers introduced the intermittency factor γ into the expression of turbulent viscosity:

$$\nu_t = \gamma \nu_t^*, \tag{1}$$

where ν_t^* is the turbulent viscosity from one of the conventional eddy-viscosity models, in order to control the growth of transition through the level of turbulent shear stress and, consequently, the production of turbulence. For example, Huang & Xiong (1998) chose the γ experimentally correlated by Dhawan & Narasimha (1958) and combined it with Menter's SST model (1993) for low-speed turbine flows. Steeland & Dick (1996), on the other hand, performed the 'conditioned-averaging' on the Navier-Stokes equation, which was split into turbulent and nonturbulent parts. Both parts together with a transport equation for γ were solved simultaneously for flows subjected to favorable/adverse pressure gradients. Recent LES for bypass transitional flow (Yang *et al.*, 1994) suggested that v' – the turbulence fluctuation in the wall-normal direction – plays an important role within the transition process. This motivates us to apply the v^2-f model (Durbin, 1995), without the inclusion of γ at the present stage, to transitional flows, in which both bypass transition and separated-flow transition involve.

The v^2-f model consists of three transport equations for the turbulent kinetic energy k, the dissipation of the turbulent kinetic energy ϵ, and a transport equation for the energy of the fluctuations normal to the streamlines $\overline{v}^2$. In addition, the model includes a Helmholz type equation for a quantity f which models the pressure-strain term. This equation is elliptic in nature, and as a consequence information from all spatial directions is used to compute the variable f at a given point. In regions of transonic flows where the velocity exceeds the speed of sound, only information from the upstream direction is needed to compute mean flow parameters. In addition, any shock waves appearing in the flow may induce strong spatial gradients in the source terms of the turbulent model. This raises the questions of whether the elliptic relaxation model is able to represent transonic flows and how accurate it is in predicting the shock location in flows involving shock-boundary layer interactions. This forms the second part of the present investigation.

2. Unified approach of v^2-f model

The turbulent velocity and time scales, L and T, are determined from the standard $k-\varepsilon$ equations:

$$\partial_t k + U \cdot \nabla k = P_k - \varepsilon + \nabla \cdot [(\nu + \frac{\nu_t}{\sigma_k})\nabla k], \tag{2}$$

$$\partial_t \varepsilon + U \cdot \nabla \varepsilon = \frac{C_{\varepsilon 1} P_k - C_{\varepsilon 2}\varepsilon}{T} + \nabla \cdot [(\nu + \frac{\nu_t}{\sigma_\varepsilon})\nabla \varepsilon]. \tag{3}$$

where T and L (to be used later) are:

$$T = \max\left[\frac{k}{\varepsilon}, 6\big(\frac{\nu}{\varepsilon}\big)^{1/2}\right],\ L = C_L \max\left[\frac{k^{3/2}}{\varepsilon}, C_\eta\big(\frac{\nu^3}{\varepsilon}\big)^{1/4}\right]. \tag{4}$$

In order to avoid the stagnation anomaly, the realizability constraints are imposed on both scales (Durbin, 1996):

$$T \le \frac{k}{\sqrt{3}\,\overline{v^2}C_\mu}\frac{1}{\sqrt{2S_{ij}S_{ij}}},\quad L \le \frac{k^{3/2}}{\sqrt{3}\,\overline{v^2}C_\mu}\frac{1}{\sqrt{2S_{ij}S_{ij}}} \tag{5}$$

where $S_{ij} = \frac{1}{2}(\frac{\partial U_i}{\partial x_j} + \frac{\partial U_j}{\partial x_i})$. On no-slip boundaries, $y \to 0$,

$$k = 0,\ \varepsilon \to 2\nu\frac{k}{y^2}. \tag{6}$$

The $\overline{v^2}$ transport equation is

$$\partial_t \overline{v^2} + U \cdot \nabla \overline{v^2} = \underline{kf - \overline{v^2}\frac{\varepsilon}{k}} + \nabla \cdot [(\nu + \frac{\nu_t}{\sigma_k})\nabla \overline{v^2}], \tag{7}$$

where

$$kf = \phi_{22} - \varepsilon_{22} + \frac{\overline{v^2}}{k}\varepsilon \tag{8}$$

represents redistribution of turbulence energy from the streamwise component. Non-locality is represented by solving an *elliptic relaxation* equation for f:

$$L^2\nabla^2 f - f = \frac{1}{T}(C_1 - 1)\left[\frac{\overline{v^2}}{k} - \frac{2}{3}\right] - C_2\frac{P_k}{k}, \tag{9}$$

The asymptotic behavior of ϕ_{22} and ε_{22} near a wall are (see, for example, Mansour *et al.*,1988):

$$\phi_{22} = -2\frac{\overline{v^2}}{k}\varepsilon,\quad \varepsilon_{22} = 4\frac{\overline{v^2}}{k}\varepsilon. \tag{10}$$

where y is minimum distance to walls. This yields the boundary condition for f:

$$kf(0) \to -5\frac{\overline{v^2}}{k}\varepsilon \ \text{ or } \ f(0) \to -\frac{20\nu^2\overline{v^2}}{\varepsilon(0)y^4} \tag{11}$$

(Durbin, 1995)

The Boussinesq approximation is used for the stress-strain relation:

$$\frac{\overline{u_i u_j}}{k} - \frac{2}{3}\delta_{ij} = -\frac{\nu_t}{k}\left(\frac{\partial U_i}{\partial x_j} + \frac{\partial U_j}{\partial x_i}\right), \tag{12}$$

where the eddy viscosity is given by

$$\nu_t = C_\mu \overline{v^2} T. \tag{13}$$

The original boundary condition for f, i.e. Eq. (11), involves $\varepsilon(0)$ in the denominator, which is ill-defined in the laminar and transitional regions. This causes oscillations for $f(0)$ in those regions as illustrated in Fig. 1 for a boundary-layer flow over a flat plate. As the flow becomes fully turbulent further downstream, $f(0)$ is well-defined and its distribution becomes fairly smooth. Note that the oscillatory behavior of $f(0)$ does not in any way influence the laminar flow solution, which is governed mainly by the molecular viscosity of the fluid. This problem, most often encountered when a segregated numerical procedure is adopted, can be overcome by reformulating the underlined term of Eq. (7) as follows:

$$\underbrace{\phi_{22} - \varepsilon_{22} + 6\frac{\overline{v^2}}{k}\varepsilon}_{=kf} - 6\frac{\overline{v^2}}{k}\varepsilon, \tag{14}$$

which changes slightly the definition of f. Important to know here is that such a modification also ensures that $\overline{v^2} \sim y^4$ as $y \to 0$. As $y \to \infty$, the kinematic blocking effect arising from 'elliptic relaxation' should disappear, i.e. both $kf - \frac{\overline{v^2}}{k}\varepsilon$ in Eq. (7) and $kf - 6\frac{\overline{v^2}}{k}\varepsilon$ in Eq. (14) should be identical and equal to

$$-C_1\frac{\varepsilon}{k}\left(\overline{v^2} - \frac{2}{3}k\right) - C_2 P_k. \tag{15}$$

Therefore, the use of $kf - 6\frac{\overline{v^2}}{k}\varepsilon$ requires the source term of Eq. (9) to be changed to:

$$\frac{1}{T}\left[(C_1 - 6)\frac{\overline{v^2}}{k} - \frac{2}{3}(C_1 - 1)\right] - C_2\frac{P_k}{k}. \tag{16}$$

To facilitate the coding, two variants of the $v^2 - f$ model are combined into the same set of equations:

$$\partial_t \overline{v^2} + U \cdot \nabla \overline{v^2} = kf - n\overline{v^2}\frac{\varepsilon}{k} + \nabla \cdot \left[\left(\nu + \frac{\nu_t}{\sigma_k}\right)\nabla \overline{v^2}\right], \tag{17}$$

$$L^2 \nabla^2 f - f = \frac{1}{T}\left[(C_1 - n)\frac{\overline{v^2}}{k} - \frac{2}{3}(C_1 - 1)\right] - C_2\frac{P_k}{k}, \tag{18}$$

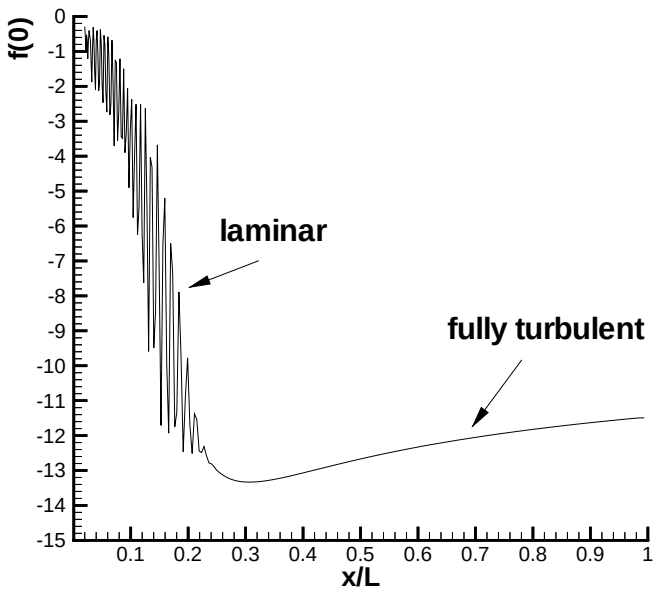

FIGURE 1. Distribution of $f(0)$ for a flow over a flat plate.

where $n = 1$ corresponds to the original $v^2 - f$ model and $n = 6$ relates to the variant of the model discussed in Lien & Durbin (1996). The constants of the original model (i.e. $n = 1$) are:

$$C_\mu = 0.22,\ \sigma_k = 1,\ \sigma_\varepsilon = 1.3,$$

$$C_{\varepsilon 2} = 1.9,\ C_1 = 1.4,\ C_2 = 0.3 \tag{19}$$

$$C_{\varepsilon 1} = 1.4(1 + 0.045\sqrt{k/\overline{v^2}}),\ C_L = 0.25,\ C_\eta = 80. \tag{20}$$

For $n = 6$, $C_{\varepsilon 1},\ C_L,\ C_\eta$ needs a slight adjustment:

$$C_{\varepsilon 1} = 1.4(1 + 0.050\sqrt{k/\overline{v^2}}) + \underline{0.4\exp(-0.1R_t)},\quad C_L = 0.23,\quad C_\eta = 70, \tag{21}$$

where $R_t = k^2/\varepsilon\nu$. The underlined term above is introduced to improve the prediction of bypass transition (see Section 4.1 for details), and its effect on the solution in the fully turbulent region is insignificant as illustrated in Fig. 2 for a fully-developed channel flow at $Re_\tau = 395$ (Kim *et al.*, 1987).

3. Numerical method

All transitional flows in Sections 4.1 and 4.2 have been computed with the STREAM general geometry, block-structured, finite-volume code (Lien *et al.*, 1996). Advection is approximated by a TVD scheme with the UMIST limiter (Lien & Leschziner, 1994). To avoid checkerboard oscillations within the co-located storage

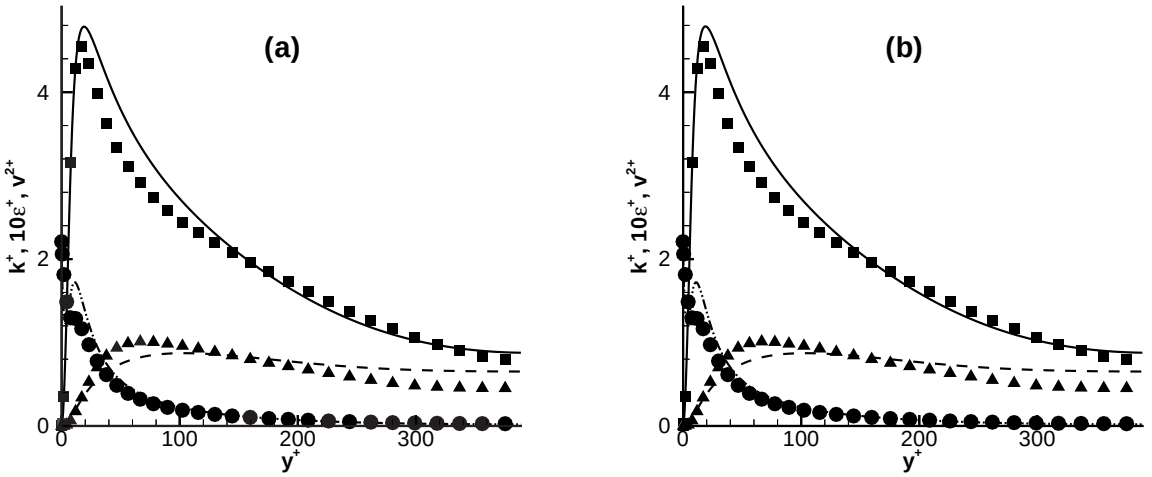

FIGURE 2. Channel flow: (a) with $0.4\exp(-0,1R_t)$ in $C_{\varepsilon 1}$; (b) without $0.4\exp(-0,1R_t)$ in $C_{\varepsilon 1}$; ——— k^+(comp); —·—·— $10\varepsilon^+$(comp); - - - - $\overline{v^2}^+$(comp); ■ k^+(DNS); ● $10\varepsilon^+$(DNS); ▲ $\overline{v^2}^+$(DNS).

arrangement, the "Rhie and Chow" interpolation method (1983) is used. The solution is effected by an iterative pressure-correction SIMPLE algorithm applicable to both subsonic and transonic conditions.

The transonic computations in Section 4.3 were performed with the CFL3D computer code (Krist *et al.*, 1998), which solves the time-dependent thin-layer Reynolds-averaged Navier Stokes equations using multi-block structured grids. A semi-discrete finite-volume approach is used for the spatial discretization. The convective and diffusion terms are discretized with a third order upwind and a central difference stencil, respectively. The code uses flux-difference splitting based on the Roe-scheme. Time advancement is implicit. Approximate factorization is used to invert the mean flow system of equations. The steady-state computations have been performed by marching in time from an initial guess. Multigrid and local time stepping are used for convergence acceleration.

The $v^2 - f$ model is solved separately from the mean flow. The k and ϵ equations as well as the $\overline{v^2}$ and f equations are solved pairwise simultaneously. First-order upwind discretization of the convective terms has been employed. The time integration of the equations is implicit. The boundary conditions are also treated implicitly. Approximate Factorization (AF) and the Generalized Minimum Residual (GMRES) (Saad, 1986) algorithm are used to invert the resulting matrices. While the latter is more robust, it requires more computational memory. The AF method decomposes the matrices formed by the implicit operator into 1D tridiagonal matrices. This allows a very fast inversion of the matrices with very low memory requirements. The splitting, however, is an approximation and introduces error terms which necessitate smaller timesteps.

4. Results and discussion

4.1 Flow over a flat plate with a sharp leading edge at zero pressure gradient

The first problem investigated here is the simplest (though fundamentally important) transitional-flow test cases proposed in the European Research Community On Flow Turbulence And Combustion (ERCOFTAC) Special Interest Group on Transitional Modeling, which include cases T3A, T3A-, T3B, T3B+ and $\mathrm{T3B_{DNS}}$ (see Savill, 1993, for details). Two cases, namely T3A and T3A-, will be presented and the corresponding initial conditions are given in the following table:

T3A	$Tu = 3\%$	U_∞ =19.6 m/s	$l_{\varepsilon\infty}$ =5.2 mm	at x=-150 mm
T3A-	$Tu = 0.9\%$	U_∞ =5.2 m/s	$l_{\varepsilon\infty}$ =10.4 mm	at x=-150 mm

The computation domain extends to 0.15 m upstream of leading edge, allowing the free-stream turbulence quantities to be specified as the in-flow condition:

$$k_{in} = 1.5(Tu\, U_\infty)^2, \quad \varepsilon_{in} = \frac{k_{in}^{3/2}}{l_{\varepsilon\infty}} \tag{22}$$

The computational mesh for T3A, containing 200×50 nodes, is employed here, in which sufficient number of grid lines are clustered towards the leading edge. As the turbulence transport plays an important role in triggering the bypass transition, it is crucial to use a second-order convection scheme for both momentum and turbulence quantities (Chen *et al.*, 1998a).

Predicted skin-friction distributions for T3A and the corresponding profiles of mean-velocity and turbulence-intensity u' at three locations across the laminar, transitional, and fully-turbulent regions are given in Figs. 3-5. As seen from Fig. 3, the introduction of the transition-correction term $0.4\exp(-0.1R_t)$ to $C_{\varepsilon 1}$ significantly improves the prediction of the onset of transition. As a result, the U-profile within the transition zone (x=595 mm) is better predicted in comparison with the original model. Although the new R_t-dependent term in $C_{\varepsilon 1}$ does better predict the location of the peak value of u', the level of turbulence intensity is too low, particularly at x=595 mm. This discrepancy is partially due to the use of Boussinesq stress-strain relation, in which turbulence intensities are assumed to be locally isotropic ($\sim \frac{2}{3}k$). The new R_t-dependent term also acts to further suppress the u' level by increasing slightly the value of $C_{\varepsilon 1}$ near the wall, which suppresses the generation of turbulence energy and, consequently, delays the onset of transition. It is clear that the mechanisms of triggering and controlling the evolution of transition process are different in the experiment and in the model. The LES work of Yang *et al.* (1994) suggested that u' and v' are not well correlated within the transition region. So far only the LES results are able to predict the correct peak of u' within the laminar and transition regions.

The skin-friction distribution for T3A- case, of which the level of free-stream turbulence intensity and dissipation-rate length scale are lower than T3A, is given in Fig. 6. As seen, the onset of transition is too early, and the sensitivity of the

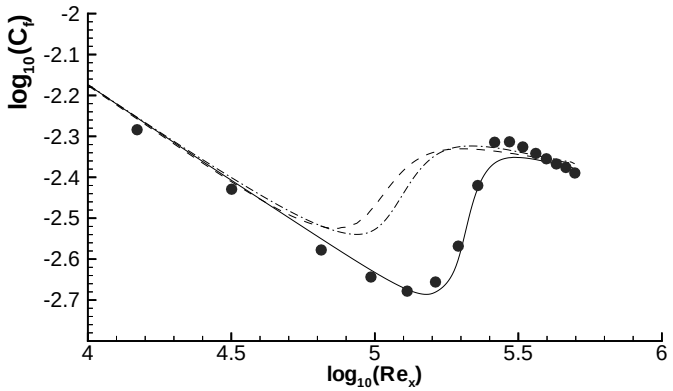

FIGURE 3. Flat plate (T3A): skin-friction distributions. ——— n=6 with R_t correction; —·— n=6 without R_t correction; - - - - n=1 (original model); • expt.

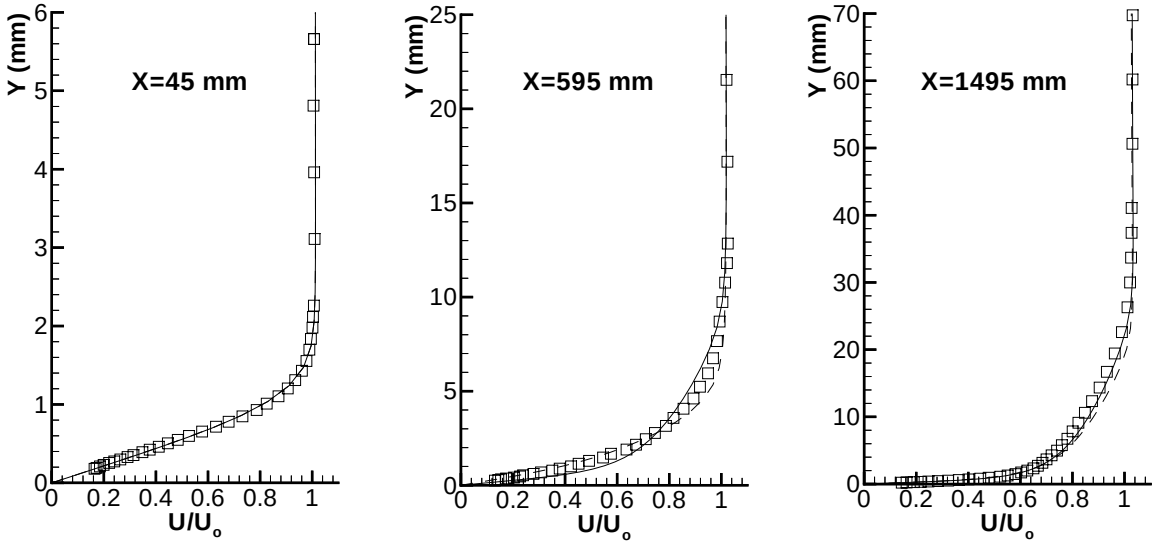

FIGURE 4. Flat plate (T3A): streamwise velocity profiles. - - - - n=6 with R_t correction; ——— n=1 (original model); ▫ expt.

R_t-dependent term to very low turbulence intensity is too weak. One possible reason for this is that at $Tu = 0.9\%$ the influence of Tollmien-Schlichting waves might not be entirely negligible. The results suggest that the dissipation equation and, likely, the 'elliptic relaxation' equation, which is responsible for energy redistribution among different Reynolds-stress components, require further re-calibration, particularly within the transition region. The introduction of intermittency factor γ into the model will increase the model's sensitivity to a number of flow features such as pressure gradients and free-stream turbulence level, depending on how γ is correlated. To pursue this modeling approach further, the provision of DNS data is indispensable.

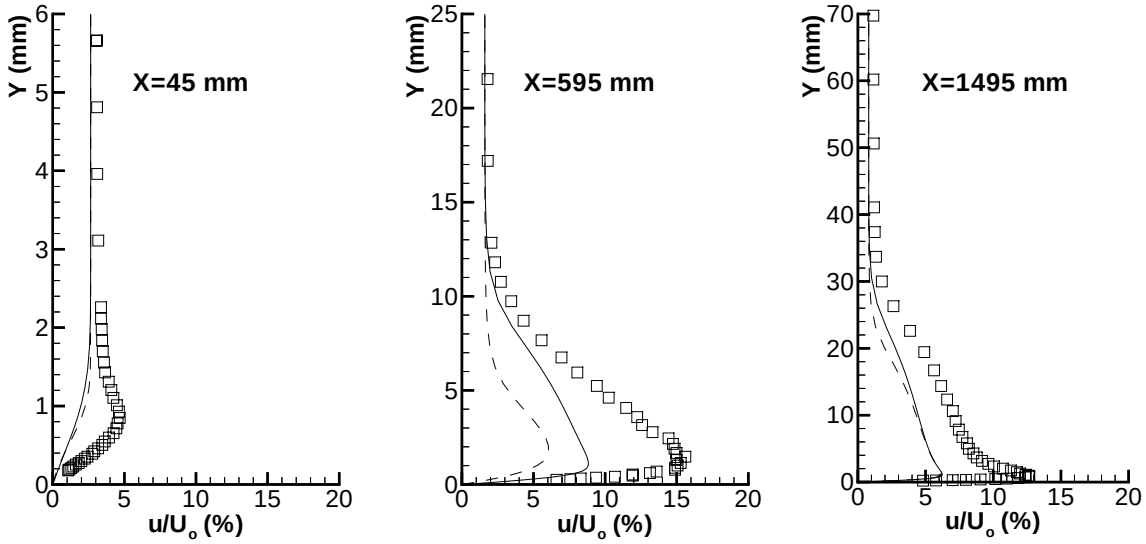

FIGURE 5. Flat plate (T3A): streamwise turbulence-intensity profiles. ---- n=6 with R_t correction; —— n=1 (original model); □ expt.

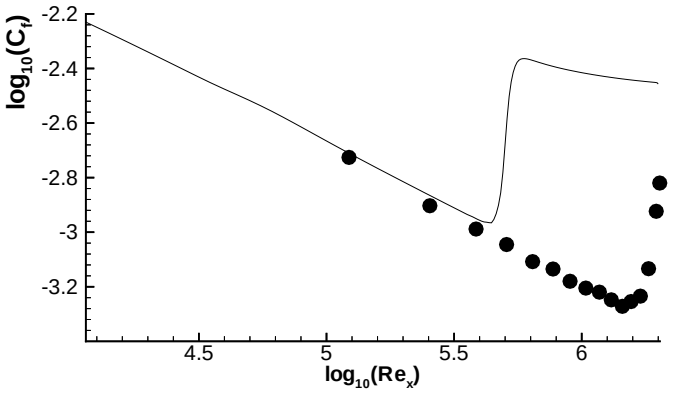

FIGURE 6. Flat plate (T3A-): skin-friction distributions. —— n=6 with R_t correction; • expt.

4.2 Double-circular-arc (DCA) compressor blade

The experimental data for DCA compressor blade was obtained by Deutsch & Zierke (1988) using one-component LDV system. The blade is formed by two circular arcs and has a 65° camber angle, a 20.5° stagger angle, a solidity of 2.14, and a 228.6 mm chord length. Three incidence angles were measured and only $i = +5°$ – the one with massive trailing-edge separation as illustrated in Fig. 7 – is considered here. The Reynolds number, based on the inlet velocity and blade chord length, is 505,000. The turbulence intensity and length scale, recommended by Chen *et al.* (1998b) and used herein, are $Tu = 2\%$ and $l_{\varepsilon\infty}$= 4.5 mm, which give the correct turbulence level at the edges of boundary layers in accord with the experimental

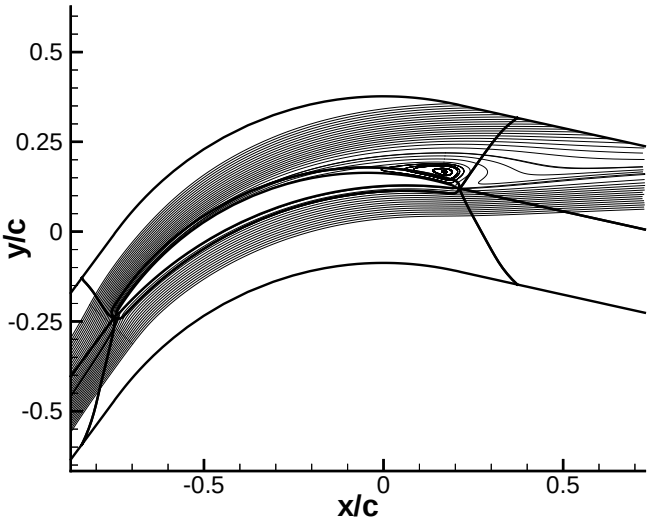

FIGURE 7. DCA compressor blade: massive trailing separation.

data. An 8-block computational mesh of 25,000 nodes, which surrounds the blade and extends in the cross-stream direction from the middle of one passage to the middle of the adjacent ones, is employed.

Experimental data suggests the existence of a large separation bubble near the leading edge. To resolve this feature, it is important to impose the realizability constraint on turbulence time and length scales in order to reduce excessive turbulence energy close to the stagnation region. The turbulence-energy contours obtained with and without the realizability constraint are shown in Fig. 8, and its impact on the size of leading-edge separation bubble are given in Fig. 9. As seen from Figs. 8 and 9, the separation bubble obtained with the realizability constraint is considerably larger than that obtained without the constraint. This is because without the constraint the turbulent mixing along the curved shear layer is too high, which entrains too much fluid into the bubble and, as a result, causes a too early reattachment.

The differences in the fluid displacement close to the leading edge also affect the development of the boundary layer further downstream. This is illustrated by the streamwise velocity profiles at two locations, $x/c = 12.7\%$ and $x/c = 94.9\%$, given in Fig. 10. The model without the realizability constraint appears to predict well the velocity profile at $x/c = 12.7\%$. However, the flow is too turbulent, which tends to resist separation. As a result, the boundary layer at $x/c = 94.9\%$ is slightly too thin. On the other hand, the use of realizability constraint overpredicts the size of leading-edge separation bubble, which results in slightly too thick boundary layers at both $x/c = 12.7\%$ and $x/c = 94.9\%$.

The distributions of pressure coefficient C_p on both sides of the blade are given in Fig. 11. The pressure plateau, clearly seen on the suction side beyond 80% of the chord, indicates that a massive trailing-edge separation exists. The model without including the realizability constraint predicts a too early pressure recovery on the

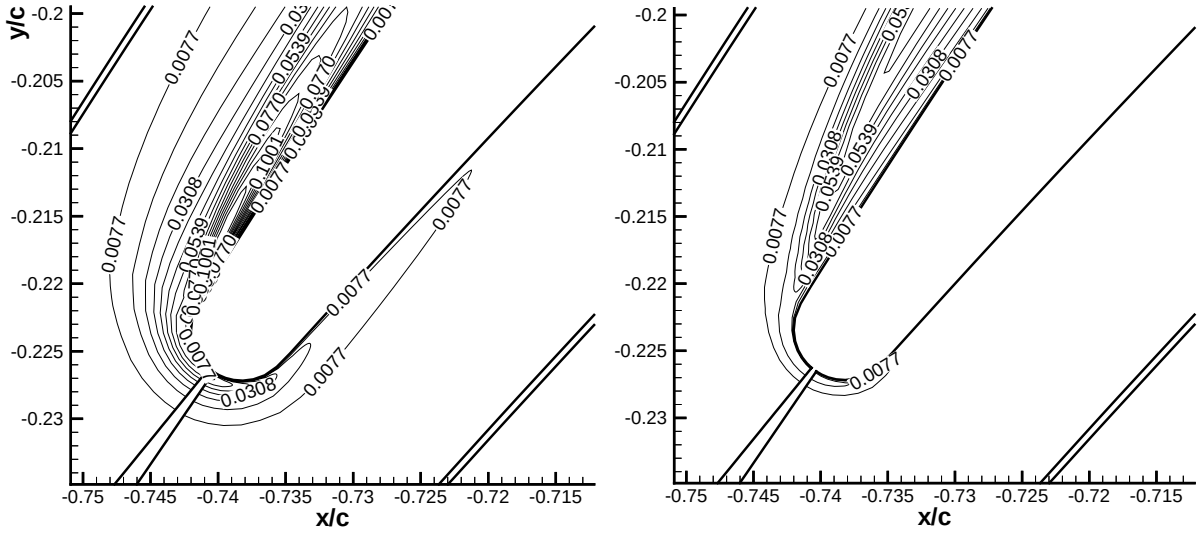

FIGURE 8. DCA compressor blade: turbulence-energy contours near the leading edge obtained without (left) and with (right) realizability constraint.

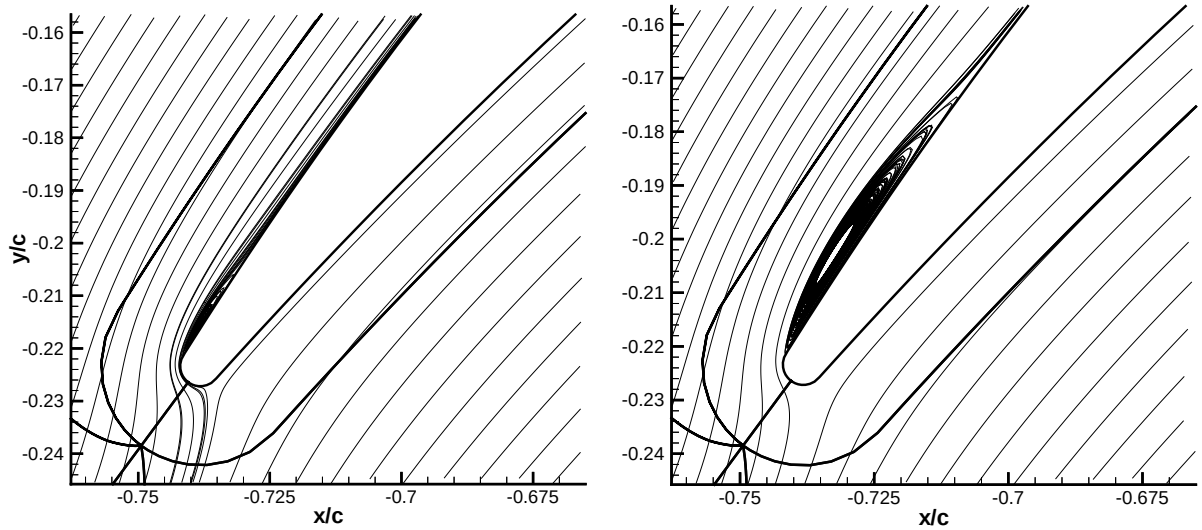

FIGURE 9. DCA compressor blade: leading-edge separation bubbles obtained without (left) and with (right) realizability constraint.

suction side, which is consistent with a too thin boundary layer at $x/c = 94.9\%$ observed in Fig. 10. Overall, it is fair to say that the results returned by the $v^2 - f$ model variants agree reasonably well with the measurement even in this complex flow involving impingement, transition, and massive separation.

4.3 RAE2822 transonic airfoil

Flow around the transonic RAE2822-airfoil has been chosen to study the performance of the $v^2 - f$ model in predicting shock-boundary layer interaction. Two test cases, case 9 and case 10, from the experiments by Cook *et al.* (1979) have been considered. The flow conditions for these cases differ only slightly in Mach and

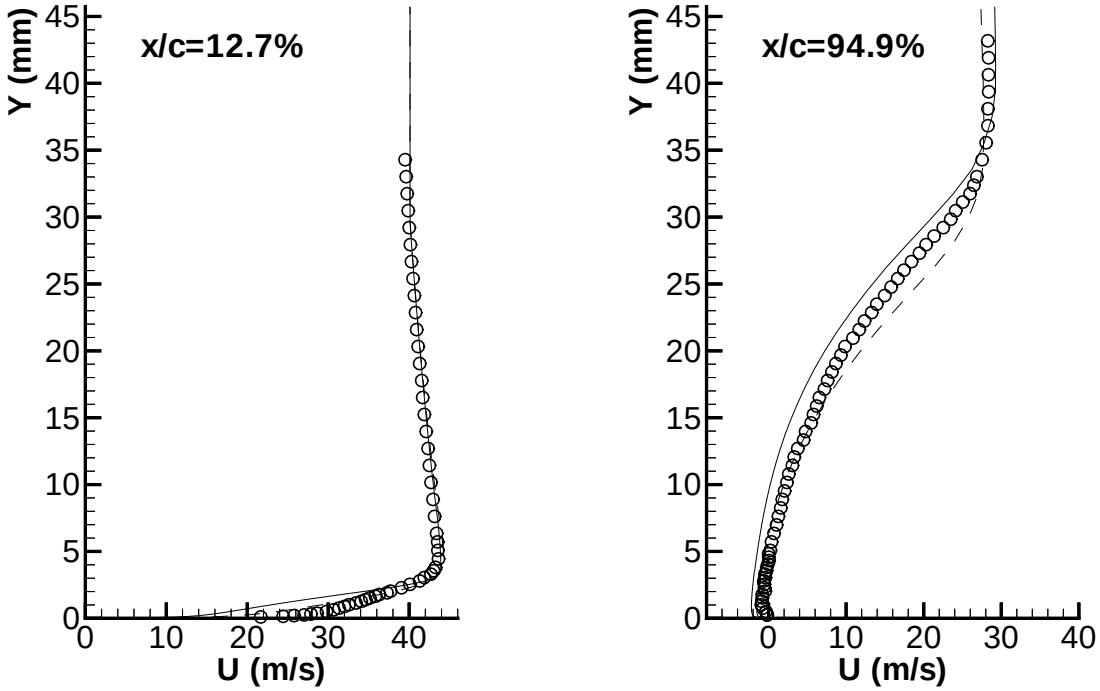

FIGURE 10. DCA compressor blade: streamwise velocity profiles. ——— n=6 with R_t correction; - - - - n=1 (original model); ∘ expt.

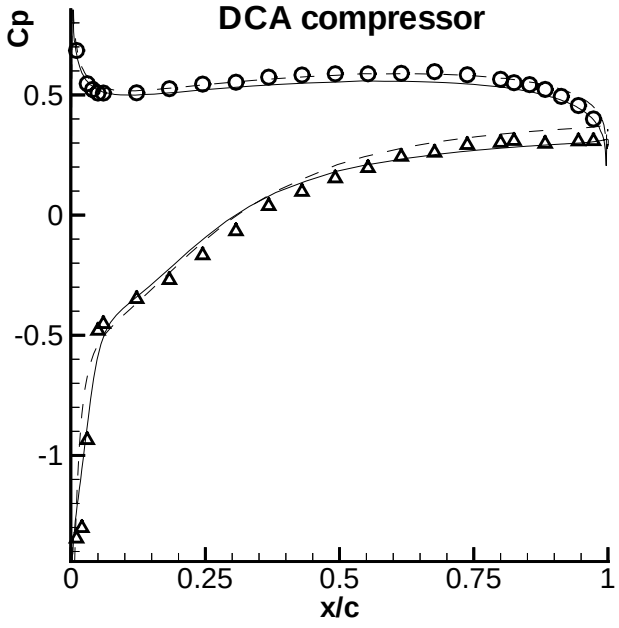

FIGURE 11. DCA compressor blade: pressure coefficient. ——— n=6 with R_t correction; - - - - n=1 (original model); ∘ expt (pressure side); △ expt (suction side).

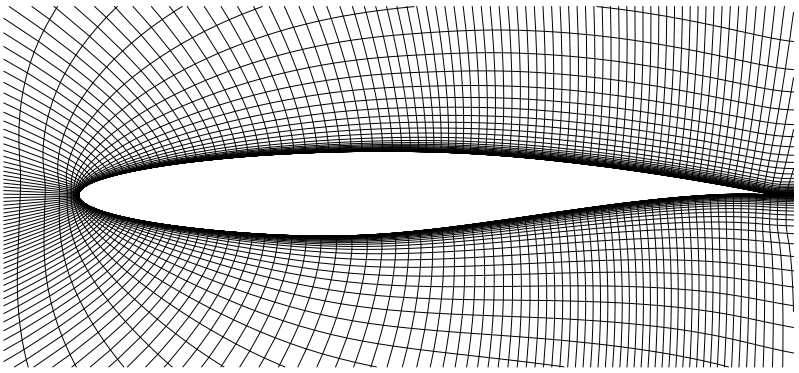

FIGURE 12. RAE2822 airfoil: computational mesh 256x64.

Reynolds number. While in case 9 the shock is too weak to induce separation, for case 10 the flow separates at the shock. The amount of separation and the position of the shock is very dependent on the turbulence model used.

The experimental data was obtained in the wind tunnel for the flow conditions: case 9: $M = 0.73, Re = 6.50\ 10^6, \alpha = 3.19^o$; and case 10: $M = 0.75, Re = 6.20\ 10^6, \alpha = 3.19^o$. Transition has been tripped in the experiments near the leading edge of the airfoil at $x/c = 0.03$ on both the upper and lower surface of the airfoil.

To compare the experimental data with the computed flow around the airfoil in free-flight conditions, corrections to the tunnel data are required. Different wind tunnel corrections have been used in the various studies published in the literature (see Haase *et al.*, 1992, Krist *et al.*, 1998, and others). The flow conditions used in the EUROVAL-project are adopted here. They are for case 9: $M = 0.734, Re = 6.50\ 10^6, \alpha = 2.54$; and for case 10: $M = 0.754, Re = 6.20\ 10^6, \alpha = 2.57$. Note that for case 10 in particular, researchers tend to compute the flow with a slightly larger angle of attack. Clearly, this influences the location of the shock. The shock location and the pressure distribution, particularly on the suction side, are influenced by the outer extent of the computational domain. The finite far field boundary causes a lower circulation around the airfoil, leading to an underprediction of lift. A vortex correction to the far-field boundary condition adjusts the circulation around the airfoil and has, therefore, been employed for the present computations.

In addition, computations have been carried out with the Spalart-Allmaras (1992) and Menter SST (1993) models to allow a comparison of results computed with the same flow solver. Both these models are included in the standard release of CFL3D, version 5.0. The $v^2 - f$ model has been implemented in CFL3D in its original form. This corresponds to setting $n = 1$ in Eqs. (17) and (18). Transition has been fixed by switching of the production terms in the equations as described in Kalitzin (1997).

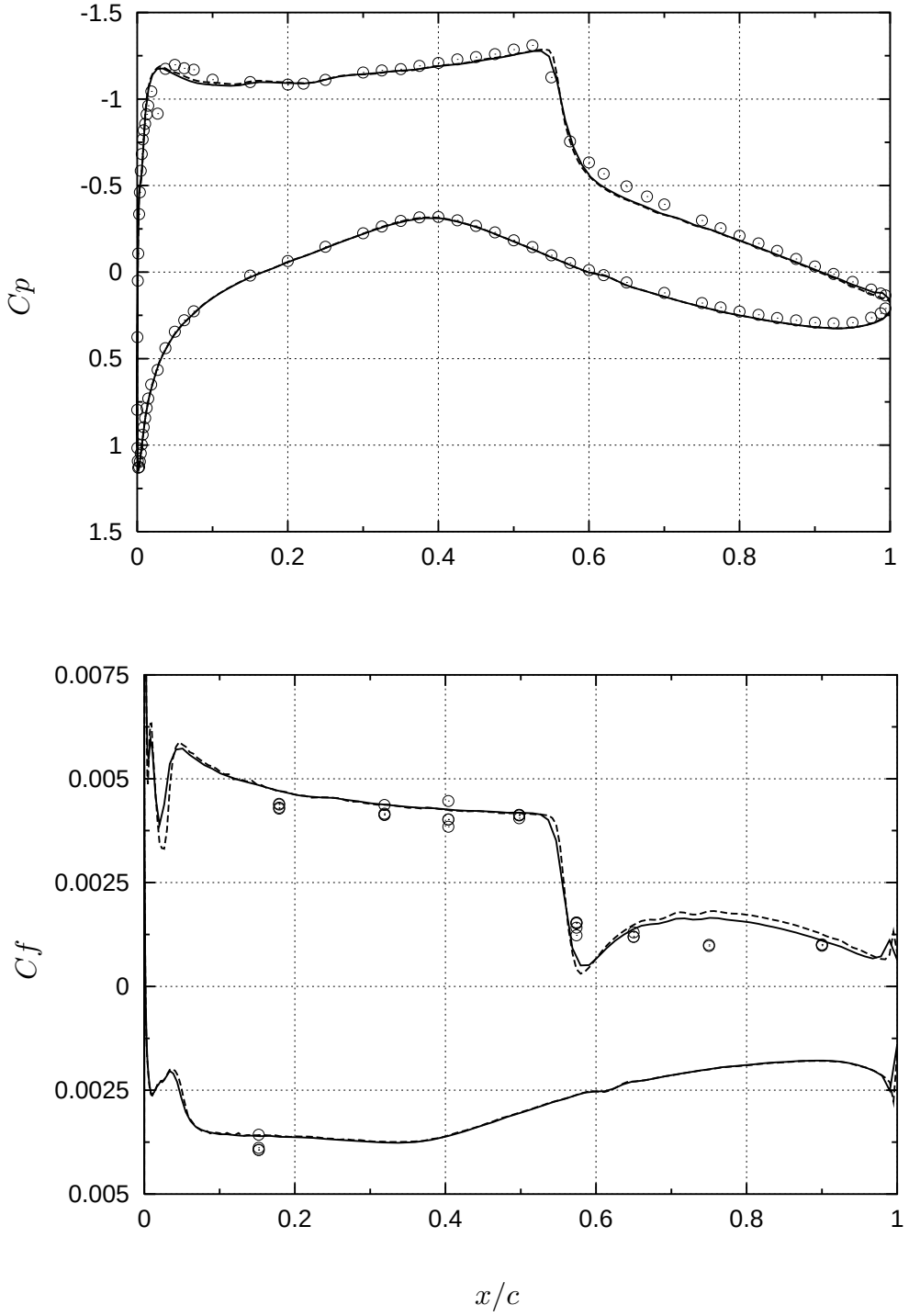

FIGURE 13. RAE2822 airfoil: pressure and skin friction distribution; case 9, ——— : $v^2 - f$ 256x64, - - - - : $v^2 - f$ 512x128, ∘ : expt.

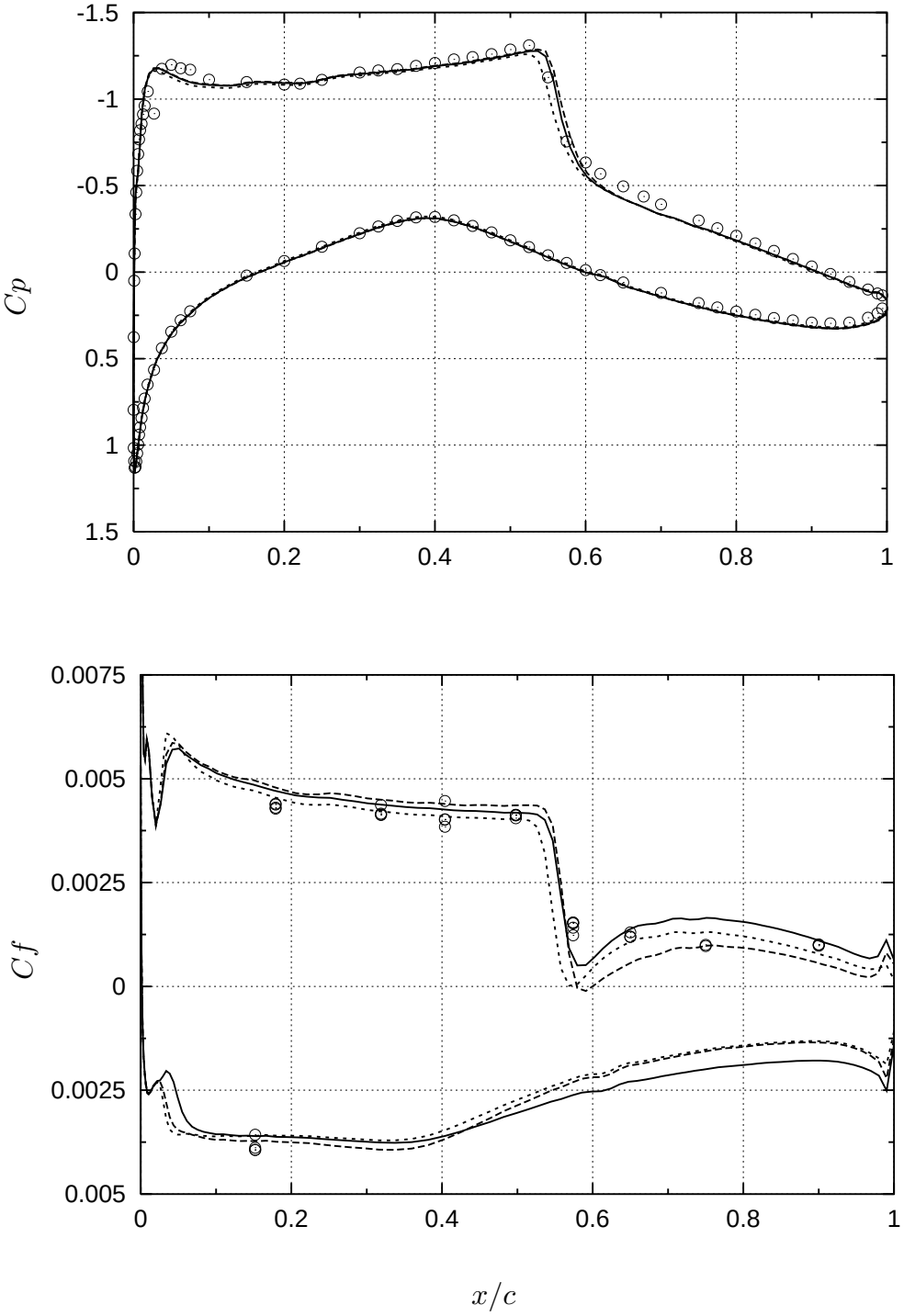

FIGURE 14. RAE2822 airfoil: pressure and skin friction distribution; case 9, ——— : $v^2 - f$, – – – – : Spalart-Allmaras, ····· : Menter SST, ○ : expt.

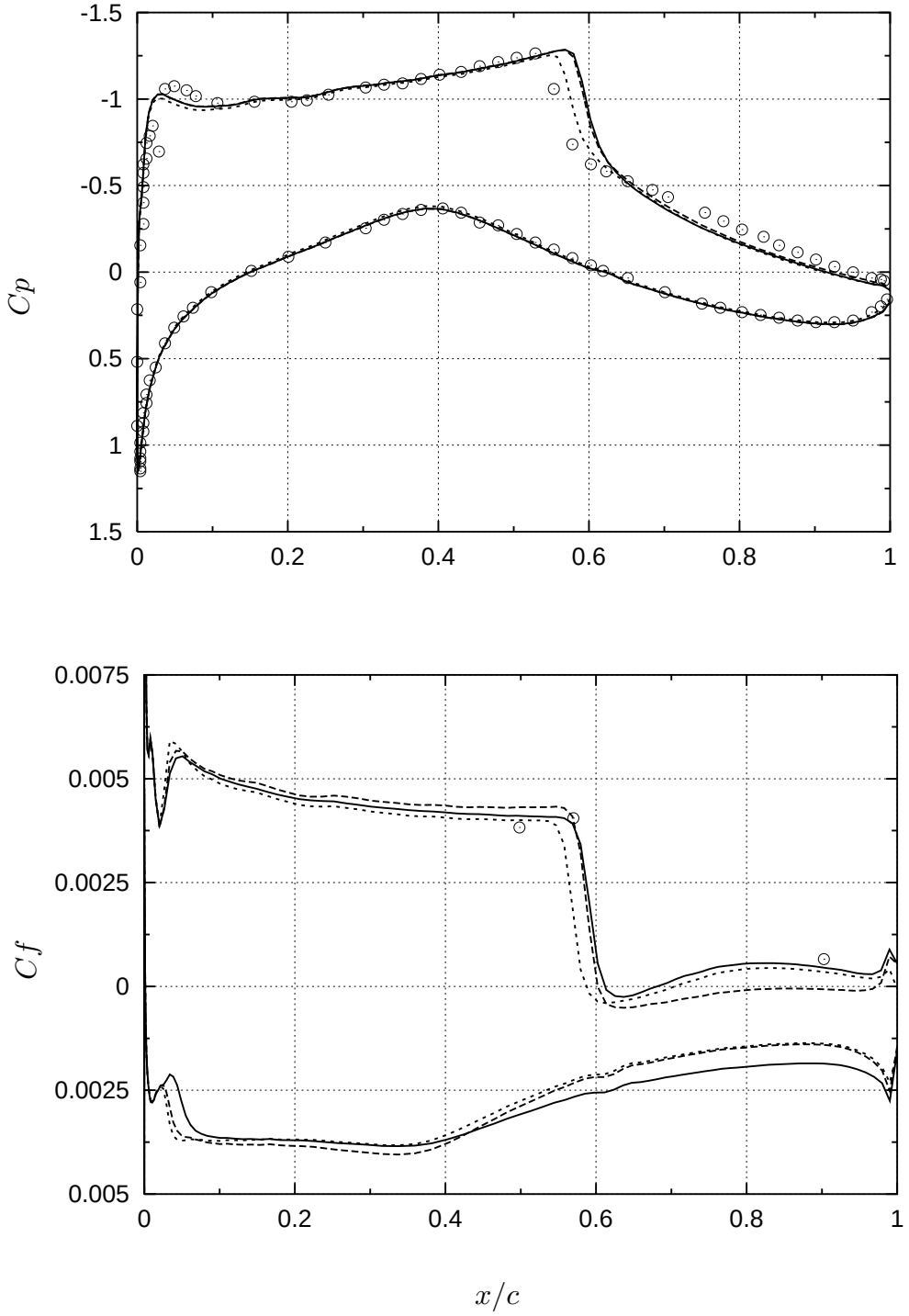

FIGURE 15. RAE2822 airfoil: pressure and skin friction distribution; case 10, ——— : $v^2 - f$, – – – – : Spalart-Allmaras, ····· : Menter SST, ○ : expt.

The present computations were carried out using the EUROVAL mesh, which consists of 256x64 cells. 192 cells are located on the airfoil surface. The far field is about 15 cord lengths from the airfoil. The average y^+ value of the first cell above the wall is about 1. The airfoil is represented in this mesh along the measured (not the designed) airfoil contours. The mesh is shown in Fig. 12.

A grid dependency study has been carried out with the $v^2 - f$ model for case 9 on a mesh with twice as many cells in each direction. The average y^+ value of the first cell above the wall is for this mesh about 0.5. The pressure and skin friction distribution is almost mesh independent as indicated by the results shown in Fig. (13).

A comparison of the pressure and skin friction distribution computed with the $v^2 - f$, the Spalart-Allmaras and the Menter SST models are shown in Figs. 14 and 15 for case 9 and 10, respectively. While the pressure distribution agrees quite well with the experimental data for all models for case 9, the shock location is generally too far downstream for case 10. The $v^2 - f$ model predicts the shock location very similarly to the Spalart-Allmaras model in both cases. It is, however, interesting to note that the skin friction computed with the Spalart-Allmaras model for case 10 reveals a fully separated flow from the shock downstream to the trailing edge. One would expect that this separation would lead to a thicker boundary layer with the consequence of a shock location further upstream. The SST model, in contrast, predicts the shock further upstream while the separation bubble is of similar size as with the $v^2 - f$ model. It is also interesting to note the similarity in the skin friction on the pressure side of the airfoil for the Menter SST and the Spalart-Allmaras models. The skin friction predicted with the $v^2 - f$ model is slightly larger here than with the other two models.

The lift and drag coefficients for case 9 and 10 are given in the table below. For the $v^2 - f$ model the predicted force coefficients lie somewhere in between the ones obtained with the Menter SST and Spalart-Allmaras models.

	$v^2 - f$ (512x128)	$v^2 - f$	Spalart-Allmaras	Menter SST	Expt
case 9					
C_L	.7983	.7995	.8066	.7789	.803
C_D	.01645	.01733	.01738	.01611	.0168
case 10					
C_L		.7570	.7628	.7262	.743
C_D		.02587	.02645	.02407	.0242

The convergence of all three models investigated for case 9 required about 1000 iterations for a 5-order magnitude drop in the L2 norm of the residual of the mean flow and turbulence quantities. In the $v^2 - f$ computation of case 10, however, small unsteady oscillations in $\overline{v^2}$ and f were observed between the shock and the trailing edge. These oscillations are caused by the use of local timesteps for the turbulence equations. The computation fully converged when a constant timestep was used throughout the boundary layer. The results presented were achieved by using local

timesteps for the mean flow and constant timesteps for the turbulence equations. This finding requires further investigation.

5. Conclusions

A unified formulation of the $v^2 - f$ model, which allows two types of boundary conditions at walls depending on the value of integer 'n', is adopted here with application to both transitional and compressible flows, the latter involving shock waves. The outcome of the present study permits the following conclusions to be drawn:

(1) In most cases (some of the results are not included here for brevity), both variants have very similar performance. The 'code-friendly' version (i.e. n=6) is numerically more robust for transitional flows when an uncoupled solution procedure is adopted.

(2) The performance of the $v^2 - f$ model for a flow over compressor-cascade blades, involving both the leading-edge and trailing-edge separation, are very encouraging. The imposition of realizability constraint on turbulence scales significantly reduces the level of turbulence energy at the stagnation region. Although the size of the resulting laminar separation bubble is slightly too large, the velocity profiles close to the trailing edge are in good agreement with the experimental data.

(3) In order to model the transition mechanism on the basis of physical ground, the intermittency effect needs to be incorporated into RANS models. The DNS data, once available, will provide detailed information in terms of the Reynolds-stress budget and intermittency factor, which can be used to re-calibrate the pressure-strain term and turbulence-dissipation equation within the transition region.

(4) Combining Dhawan & Narasimha's intermittency factor with the $v^2 - f$ model based on the conditioned Navier-Stokes equation approach is currently under investigation.

(5) The results obtained with the $v^2 - f$ model for the RAE2822 airfoil demonstrate the capability of predicting transonic flows around airfoils. The present computations were carried out with the original model setting $n = 1$. Generally, the model converges well even on the finer mesh. This is attributed to a pairwise implicit solution of the model's equations and an implicit treatment of the boundary conditions.

Acknowledgments

The first author would like to express his gratitude to CTR and University of Waterloo in Canada for their financial support.

REFERENCES

Chen, W. L., Lien, F. S. & Leschziner, M. A. 1998a Non-linear eddy-viscosity modeling of transitional boundary layers pertinent to turbomachine aerodynamics. *Int. J. Heat Fluid Flow.* **19,** 297-306.

Chen, W. L., Lien, F. S. & Leschziner, M. A. 1998b Computational prediction of flow around highly loaded compressor-cascade blades with non-linear eddy-viscosity models. *Int. J. Heat Fluid Flow.* **19,** 307-319.

Craft, T. J., Launder, B. E. & Suga, K. 1995 A non-linear eddy viscosity model including sensitivity to stress anisotropy. *Proc. 10th Symp. on Turbulent Shear Flows.* **2,** 23.19-23.24.

Cook, P. H., McDonald, M. A. & Firmin, M. C. P. 1979 Aerofoil 2822 - pressure distributions, boundary layer and wake measurements. *AGARD AR 138.*

Deutsch, S. & Zierke, W. C. 1988 The measurement of boundary layers on a compressor blade in cascade: part 2 – suction surface boundary layers. *ASME J. Turbomach..* **110,** 138-145.

Dhawan, S. & Narasimha, R. 1958 Some properties of boundary layer during the transition from laminar to turbulent flow motion. *J. Fluid Mech.* **3,** 418-436.

Durbin, P. A. 1995 Separated flow computations with the $k-\epsilon-\overline{v^2}$ model. *AIAA J.* **33,** 659-664.

Durbin, P. A. 1996 On the $k-\varepsilon$ stagnation point anomaly. *Int. J. Heat and Fluid Flow.* **17,** 89-90.

Haase, W., Bradsma F., Elsholz E., Leschziner M., & Schwamborn D. 1993 EUROVAL-an European Initiative on Validation of CFD Codes. *Notes on Numerical Fluid Mechanics, Volume 42, Vieweg.*

Huang, P. G. & Xiong, G. 1998 Transition and turbulence modeling of low pressure turbine flows. *AIAA Paper No. 98-0339.*

Kalitzin G. 1997 Application of turbulence models to high-lift airfoils. *CTR-Annual Research Briefs, Center for Turbulence Research, NASA Ames/Stanford Univ., 165-177.*

Kim, J., Moin, P. & Moser, R. D. 1987 Turbulence statistics in fully-developed channel flow at low Reynolds number. *J. Fluid Mech.* **177,** 133-166.

Krist, S., Biedron, R. & Rumsey, C. 1998 CFL3D User's Manual (Version 5.0). *NASA/TM-1998-208444.*

Launder, B. E. & Sharma, B. I. 1974 Application of the energy dissipation model of turbulence to the calculation of flow near a spinning disc. *Letters in Heat and Mass Transfer.* **1,** 131-138.

Lien, F. S. & Durbin, P. A. 1996 Non-linear $k-\varepsilon-v^2$ modeling with application to high-lift. *CTR summer proceedings*

Lien, F. S. & Leschziner, M. A. 1994 Upstream monotonic interpolation for scalar transport with application to complex turbulent flows. *Int. J. Num. Methods Fluids.* **19,** 527-548.

Lien, F. S., Chen, W. L. & Leschziner, M. A. 1996 A multiblock implementation of a non-orthogonal collocated finite volume algorithm for complex turbulent flows. *Int. J. Num. Methods Fluids.* **23,** 567-588.

Mansour, N. N., Kim, J. & Moin, P. 1988 Reynolds-stress and dissipation-rate budgets in a turbulent channel flow. *J. Fluid Mech.* **194,** 15-44.

Menter, F. R. 1993 Zonal two equation $k-\omega$ turbulence model predictions. *AIAA Paper No. 93-2906.*

Rhie, C. M. & Chow, W. L. 1983 Numerical study of the turbulent flow past an airfoil with trailing edge separation. *AIAA J.* **21,** 1525-1532.

Saad, Y. & Schultz M. H. 1986 GMRES: a generalized minimal residual algorithm for solving nonsymmetric linear systems. *SIAM J. Sci. Stat. Comp.* **7,** 856-869.

Savill, A. M. 1993 Some recent progress in the turbulence modeling of bypass transition. *Near-Wall Turbulent Flows. R. M. C. So, C. G. Speziale & B. E. Launder (eds.) 829-848, Elsevier Science Publishers.*

Steelant, J. & Dick, E. 1996 Modeling of bypass transition with conditioned Navier-Stokes equations coupled to an intermittency transport equation. *Int. J. Num. Methods Fluids.* **23,** 193-220.

Spalart, P. R. & Allmaras, S. R. 1992 A one-equation turbulence model for aerodynamic flows. *AIAA Paper No. 92-439.*

Yang, Z., Voke, P. R. & Savill, A. M. 1994 Mechanism and models of boundary layer receptivity deduced from large-eddy simulation of bypass transition. *Direction and Large-Eddy Simulation.* **1,** P. R. Voke, L. Kleiser & J. Chollet (eds.) 225-236, Kluwer Academic Publishers.